



Optimizing hydrogen evolution activity of nanoporous electrodes by dual-step surface engineering

Long Liu^{a,1}, Di Li^{b,1}, Huaping Zhao^{a,*}, Anna Dimitrova^a, Longhua Li^b, Yaoguo Fang^{a,b}, Stefan Krischok^a, Weidong Shi^{b,*}, Yong Lei^{a,*}

^a Institut für Physik & IMN MacroNano (ZIK), Technische Universität Ilmenau, Ilmenau 98693, Germany

^b Institute for Energy Research, School of Chemistry and Chemical Engineering, Jiangsu University, Zhenjiang 212013, China



ARTICLE INFO

Keywords:

Hydrogen evolution reaction
Nanoporous electrode
Surface engineering
Cobalt nanopore arrays
Wettability

ABSTRACT

The hydrogen evolution reaction (HER) from electrocatalytic water splitting represents an important approach for efficient hydrogen production, in which the HER feasibility relies on electrocatalysts as well as the art of electrode design. Herein, a considerate surface engineering strategy is developed for promoting HER process taking place on nanoporous HER electrodes. Cobalt nanopore arrays (CoNPA) are fabricated as the representative nanoporous HER electrode. Then an ultrathin titanium dioxide (TiO_2) with optimized thickness is conformally coated onto CoNPA for improving the wettability in order to expose more active sites, followed by a well-dispersed platinum (Pt) nanoparticles with an ultralow mass loading (ca. $54 \mu\text{g cm}^{-2}$) anchored on TiO_2 layer for enhancing the HER activity. The advanced features of nanoporous architecture in combination with the synergistic contribution from ultrathin TiO_2 layer and well-dispersed Pt nanoparticles enable CoNPA@ TiO_2 @Pt electrode exhibit outstanding HER performance in alkaline conditions, *i.e.*, an overpotential of 29 mV needed to reach the catalytic current density of 10 mA cm^{-2} and long-term performance as well as structure stability. Not limited to the HER electrodes, the similar strategy is also expected to be further applied to the rational design and nanoengineering of electrodes for other electrochemical energy conversion and storage devices.

1. Introduction

Hydrogen represents one of the most promising energy carriers of the future with the merits of environmental benignity and high energy efficiency [1]. In comparison to current hydrogen production technology that primarily relies on the steam methane reforming process, the evolution of hydrogen from electrochemical water splitting bears great potentials as a sustainable approach for hydrogen production [2]. Generally, efficient water splitting requires electrocatalysts with high activity and durability to promote the hydrogen evolution reaction (HER). Up to now, platinum (Pt) based noble metals are the most efficient and robust HER electrocatalysts except for their scarcity and costliness [3,4]. Thus, tremendous efforts are devoted to either the improvement of utilization efficiency for Pt based noble metals or the explorations of novel noble-metal-free HER electrocatalysts such as non-noble metals/alloys [5–9] as well as transition metal oxides [10–13], sulfides [14–20], phosphides [21–25], carbides [26–29], and borides [30,31] to replace precious Pt [32]. In addition to the dependence on materials engineering for the electrocatalysts [33], the

ultimate HER efficiency also partially depends on the art of HER electrode design [34,35]. As known, HER is a multi-step electrochemical process carrying out on the surface of the electrocatalysts, and it generally involves: electrochemical hydrogen adsorption (Volmer reaction) through water dissociation and the resultant reactive intermediates (H^* atoms) are chemically adsorbed on the surface of electrocatalysts, followed by chemical desorption (Tafel reaction) or electrochemical desorption (Heyrovsky reaction) to form molecular hydrogen by the recombination of H^* atoms chemically adsorbed on the electrocatalyst surface [36]. Therefore, an promising HER electrode principally should have ample and accessible active centers, high electrical conductivity, and optimized electrode geometry, *etc.* [37].

Three-dimensional (3D) nanoarchitected electrodes design now becomes of significant importance mainly attributing to the high specific surface area, offering great opportunities for the exposure of more active centers [38,39]. So far many 3D nanoarchitected HER electrodes have been designed, fabricated, and intensively investigated aiming at achieving highly-efficient HER activity [40]. It has been specifically pointed out that confining or decorating active sites into

* Corresponding authors.

E-mail addresses: huaping.zhao@tu-ilmenau.de (H. Zhao), swd1978@ujs.edu.cn (W. Shi), yong.lei@tu-ilmenau.de (Y. Lei).

¹ These authors contributed equally to this work.

porous electrodes could effectively improve stability due to the unique electronic microenvironments within the semi-closed space that realize superior diffusion properties within a nanospace and modulate electron transfer processes without sacrificing the metal-support interactions [41]. It is therefore highly attractive to rational design 3D nanoarchitected HER electrodes consisting of a uniform and controlled porous structure for long-term electrocatalytic hydrogen production with high efficiency. When designing 3D nanoarchitected, or more specifically, nanoporous HER electrodes, a good wettability should be a cause for concern in order to enable expose ample and water-accessible active centers for HER process [42]. But at the same time, the improvement in wettability should not deteriorate the HER kinetics. Surface functionalization is normally conducted to modulate the surface wettability. Nevertheless, surface functionalization to HER electrodes will inevitably affect more or less on the electrochemical nature of the electrocatalyst surface accompanying with the reform in wettability, and thus might impose either positive or negative effects on the final HER kinetics [43,44]. According to the Sabatier principle, both Volmer and Tafel/Heyrovsky reactions have a strong dependence on the electrochemical nature of the electrocatalyst surface. The binding interactions between the electrocatalyst surface and the reactive intermediates generally should be strong enough to retain the intermediates for facilitating Volmer reaction, and meanwhile the binding interactions should be weak enough to assure a facile release of the intermediates for conducting Tafel or Heyrovsky reaction as well as the release of resultant gaseous hydrogen [4,36]. To promote the HER activity toward the improvement in catalytic efficiency, a considerate surface engineering on the HER electrodes is crucial to make sure the improvement in wettability but without compromising the HER kinetics [45].

In this work, we demonstrate a dual-step surface engineering strategy for enhancing hydrogen evolution activity of cobalt nanopore arrays (CoNPA) as the representative 3D nanoporous HER electrode. An ultrathin titanium dioxide (TiO_2) layer with an optimized thickness was conformally coated onto CoNPA resulting in the significantly improved wettability, followed by well-dispersed Pt nanoparticles with an ultralow mass loading anchored on TiO_2 layer for increasing active sites and meanwhile enhancing HER catalytic activity. Obviously, benefiting from the 3D nanoarchitecture with large surface area, fast electron transport stemming from the highly conductive CoNPA framework, good wettability for water penetration arising from the conformally ultrathin TiO_2 layer, open-channels of CoNPA for effective gas release, and the catalytic contributions from Pt nanoparticles, the heterostructured CoNPA@ TiO_2 @Pt electrode exhibited high HER performance in an alkaline solution with a low overpotential of 29 mV, a small Tafel slope of 42 mV per decade as well as a long-term performance and structure stability. Furthermore, the similar dual-step surface engineering strategy demonstrated here shall be universal to be extended in other kinds of nanoarchitected HER electrodes and even for optimizing nanoarchitected electrodes for other electrochemical energy conversion and storage devices.

2. Experimental section

2.1. Fabrication of CoNPA

CoNPA was fabricated by the following steps *via* a facile AAO template-assisted method [46]. Specifically, rectangular patterned AAO template with anodization time of 60 min [47,48]. A thin gold layer (20 nm thick) was deposited onto AAO templates by electron beam deposition (Kurt J. Lesker PVD225). Then, a PMMA solution was drop-casted onto the AAO template to fill the pores. After drying, the AAO template was selectively removed using a 5 wt% H_3PO_4 solution to obtain rectangularly ordered arrays of PMMA nanopillars with the Au film at the bottom. Subsequently, Co was electroplated using the pre-deposited Au layer as working electrode in an electrolyte containing 0.05 M $\text{Co}(\text{Ac})_2$ and 0.5 M H_3BO_3 with a current density of 5 mA cm^{-2}

for 50 min to fully fill the gap among PMMA nanopillars. After that, a thick layer of Ni was electrochemically deposited as a conductive substrate. The electrolyte for Ni deposition was an aqueous solution containing 0.38 M $\text{NiSO}_4 \cdot 6\text{H}_2\text{O}$, 0.12 M $\text{NiCl}_2 \cdot 6\text{H}_2\text{O}$, and 0.5 M H_3BO_3 . Finally, the PMMA nanostructure was dissolved by dimethylsulfoxide and the thin Au layer was also removed to finally obtain CoNPA.

2.2. Fabrication of CoNPA@ TiO_2

CoNPA was coated with TiO_2 layer by using a SUNALE R-150 ALD system (Picosun, Finland). The deposition temperature was 300 °C, and TiCl_4 and H_2O were chosen as the precursors of Ti and O, respectively. The ALD steps were as follow: TiCl_4 was pulsed for 0.1 s and purged for 10 s, followed by a 0.8 s pulse of H_2O and purge for 10 s. This procedure was repeated 20, 60, 160 times to reach a thickness of ~1, ~3, ~8 nm, respectively, according to the growth rate of ~0.5 Å per cycle.

2.3. Fabrication of CoNPA@ TiO_2 @Pt

Pt nanoparticles deposited on CoNPA@ TiO_2 was performed by low-nitrogen-filling ALD process [49]. The precursors used for Pt growth were trimethyl(methyl cyclopentadienyl)platinum(IV) ($\text{Pt}(\text{MeCp})\text{Me}_3$) and O_2 . The temperature of Pt precursor was held at 80 °C, and the substrate temperature of samples was 300 °C. The ALD cycle consisted of $\text{Pt}(\text{MeCp})\text{Me}_3$ pulsing (1 s)-low N_2 filling (90 s)- N_2 purging (30 s)- O_2 pulsing (1 s)-low N_2 filling (90 s)- N_2 purging (30 s). This procedure was repeated 5 times. The mass loading of Pt was determined by using a Mettler-Toledo XP2 microgram balance (accuracy 0.1 µg) to be *ca.* 54 µg cm⁻² (0.59 wt%, $\text{m}_{\text{Pt}}/(\text{m}_{\text{Pt}} + \text{m}_{\text{Co}})$).

2.4. Characterizations

SEM analysis was conducted using a Hitachi S4800 field emission scanning microscopy equipped with energy dispersive X-ray detector (EDX, Thermal). XRD analysis was implemented on a 18 KW D/MAX2500 V PC diffractometer using $\text{Cu K}\alpha$ ($\lambda = 1.54 \text{ \AA}$) radiation. X-ray photoemission spectroscopy (XPS) was recorded with a SPECS SAGE spectrometer employing a focused and nonmonochromated Al $\text{K}\alpha$ source ($h\nu = 1486.6 \text{ eV}$). The pressure in the main chamber remained $1 \times 10^{-8} \text{ mbar}$ during XPS measurements of the samples. The binding energies obtained in the XPS spectral analysis were corrected for specimen charging by referencing C 1 s to 284.8 eV.

2.5. Electrochemical measurements

All the electrochemical experiments were implemented in a specially designed three-electrode set-up (Fig. S1) with a potentiostat (Bio-Logic VSP, France). The working electrodes were all CoNPA-based HER electrodes. The graphite rod and Ag/AgCl reference electrode were used as the counter and reference electrodes, respectively. All working electrodes were soaked in the electrolyte for 1 h before starting the electrochemical test in order to fully impregnate electrodes with water. For HER experiments, the linear sweep voltammograms (LSVs) were measured at a scan rate of 10 mV s^{-1} in 1 M KOH solution. All the potentials reported here were against reversible hydrogen electrode (RHE) through RHE calibration: $E_{\text{RHE}} = E_{\text{Ag/AgCl}} + 1.035 \text{ V}$ [15]. Before the electrochemical measurement, the open-circuit potential of the electrodes was determined, which are centered at 0.10–0.15 V vs. RHE. And all displayed voltammograms are *iR* corrected to account for any uncompensated resistance. It is worth noting that as the cathodic potentials are negative values, the overpotential values involved in this article are absolute ones.

To acquire the electrochemically active surface area (ECSA) of the working electrodes, their roughness factor (R_f) were obtained according to the equation: $\text{ECSA} = R_f \times S$, where S was generally equal to the geometric area of electrode (here $S = 0.5 \text{ cm}^2$). The R_f was determined

from the ratio of double-layer capacitance C_{dl} for the working electrode and the corresponding smooth metal electrode (assuming that the average double-layer capacitance of a smooth metal surface is $20 \mu\text{F cm}^{-2}$), that is, $R_f = C_{dl}/20 \mu\text{F cm}^{-2}$ [50]. The C_{dl} could be acquired by cyclic voltammetry measurement in the non-faradic region within the potential windows of $0.1 - 0.2 \text{ V vs. RHE}$ (in 1 M KOH solution). The various scan rates were utilized, such as $30, 50, 80, 100, 120, 150$, and 200 mV s^{-1} , respectively. The C_{dl} was estimated by plotting the Δj at 0.15 V (where Δj is equal to the absolute difference between cathodic and anodic current densities, respectively) vs. RHE against the scan rate, in which the slope was twice that of C_{dl} . The calculated ECSA values for different electrodes are listed in Table S1. The values of specific activity ($\text{mA cm}_{\text{ECSA}}^{-2}$) were calculated from ECSA values (cm^2) and the measured current densities j ($\text{mA cm}_{\text{geo}}^{-2}$):

2.6. Computational method

In order to elucidate the underlying reasons behind the distinct performance, the adsorption energy of H^* adsorption of CoNPA, CoNPA@TiO₂, CoNPA@Pt and CoNPA@TiO₂@Pt in alkaline solution are achieved by the computational calculations and models. All calculations were performed by density functional theory (DFT) pseudopotential plane-wave method as implemented in the Vienna ab initio simulation package (VASP) [51]. The all-electron projected augmented wave (PAW) [52,53] potential was used to describe the ion – electron interaction. The electron wave function basis set was expanded up to a cutoff energy of 400 eV . The spin-polarized GGA-PBE was adopted. A $2 \times 2 \times 1$ Monkhorst – Pack (MP) k mesh was sampled for optimization and vibration calculations. The Gibbs free energy of H^* and the vibration contributions to zero point energy (ZPE) and entropy (S) are calculated as follows:

$$\begin{aligned} G(\text{H}^*) &= \Delta E + \Delta ZPE - T\Delta S \\ &= E(\text{H}^*) - E(\text{H}) - E^* + ZPE(\text{H}^*) - ZPE(\text{H}) - ZPE^* \\ &\quad - T(S(\text{H}^*) - S(\text{H}) - S^*) \\ ZPE &= \sum_{i=1}^N \frac{\hbar\omega_i}{2} \\ S &= \sum_{i=1}^N R \left\{ \frac{\theta/T}{e^{\theta/T} - 1} - \ln(1 - e^{-\theta/T}) \right\}; \theta = \frac{\hbar\omega_i}{k_B} \end{aligned}$$

where E , ω , and R , k_B and c are the electronic total energy, frequency, gas constant, Boltzmann constant and light speed, respectively.

3. Results and discussion

The fabrication process for CoNPA@TiO₂@Pt electrode is schematically illustrated in Fig. 1a. Briefly, CoNPA was firstly fabricated as the representative 3D nanoporous HER electrode through a two-step replication process (Fig. S2) and highly-ordered anodized aluminum oxide (AAO) membranes with a rectangular pore arrangement (Fig. 1b and Fig. S3) were applied as the initial template [46,54,55]. Here, the pore diameter of AAO template was 350 nm . Then an ultrathin TiO₂ layer was conformally coated onto CoNPA by atomic layer deposition (ALD). The thickness of TiO₂ layer were controlled to be about $1, 3$, and 8 nm (Fig. S4), respectively, with the corresponding ALD cycle numbers of $20, 60$, and 160 , respectively. After that, well-dispersed Pt nanoparticles with ultralow mass loading (*ca.* $54 \mu\text{g cm}^{-2}$, determined by comparing the mass change after Pt deposition) were further anchored on ultrathin TiO₂ layer by ALD to finally produce heterostructured CoNPA@TiO₂@Pt electrode [49,56]. Fig. 1c is one representative top-view scanning electron microscope (SEM) image of the as-prepared CoNPA. As the initial AAO template, CoNPA had rectangular pore arrangement with the pore diameter of 350 nm . After conformally coated with 3-nm-thick TiO_2 , CoNPA@TiO₂ remained the main structure features as CoNPA but only the pore diameter was slightly reduced (Fig. 1d). Furthermore, negligible changes in morphology could be found from the top-view SEM image of CoNPA@TiO₂@Pt (Fig. 1e) as

compared to that of CoNPA@TiO₂ (Fig. 1d). Fig. 1f reveals that the pore depth of CoNPA in this work is about $5.5 \mu\text{m}$. The enlarged cross-sectional SEM images give more detailed information about the walls of CoNPA, CoNPA@TiO₂, and CoNPA@TiO₂@Pt. As shown in Fig. 1g, the wall surface of CoNPA is relatively rough, and becomes smooth after coated with TiO₂ layer (Fig. 1h). And it can be clearly seen from Fig. 1i that the tiny Pt nanoparticles are well-dispersed over the whole walls of CoNPA@TiO₂. The size distribution of the well-dispersed Pt nanoparticles inside the nanopore was evaluated from the high-resolution SEM image by measuring about 100 individual Pt nanoparticles. As shown in the Fig. S5, the diameter of the nanoparticles ranges from 1 to 4 nm and mainly locates at $\sim 3 \text{ nm}$. The tiny Pt nanoparticles endow the nanoarchitected electrode with ample active sites [57]. X-ray diffraction (XRD) of CoNPA@TiO₂@Pt sample clearly revealed the cobalt crystallographic structure without any peaks of impurities (Fig. S6). Notably, almost no diffractions could be ascribed to TiO₂ and Pt in all samples, which are mainly attributed to the relatively low crystallinity and low content of TiO₂ nanolayer or Pt nanoparticles within the core-shell hybrids. Moreover, energy-dispersive X-ray spectrometry (EDX) mapping of Co, O, Ti, and Pt elements distributions from the top (Fig. 1j) and cross-section of CoNPA@TiO₂@Pt (Fig. S7) further confirm the compositions of CoNPA@TiO₂@Pt and also the good dispersion of tiny Pt nanoparticles anchored on the inner wall of CoNPA@TiO₂@Pt.

As mentioned above, the nanoporous HER electrodes should have good wettability to expose more water-accessible active centers for electrochemical water splitting. The role of ultrathin TiO₂ layer here is optionally designed to improve the wettability of CoNPA [58], however, it was found that the TiO₂ layer could also impact on the HER activity of CoNPA and the impact degree was depended on the thickness of TiO₂ layer. The linear sweep voltammogram (LSV) experiments indicated that the best electrocatalytic activity of CoNPA@TiO₂ was achieved with 3-nm-thick TiO_2 layer (Fig. S8). For the CoNPA@TiO₂ electrode with 8-nm-thick TiO_2 layer, the decreased activity might be attributed to the inefficient electron transfer caused by the thick TiO₂ coating [58,59]. Hereafter, all the CoNPA@TiO₂@Pt electrodes refer to TiO₂ layer with 3 nm in thickness. Fig. 2 reveals the evolutional hydrophilic performance of the water droplets on the HER electrodes surface. CoNPA electrode had a high water contact angle of 86.8° and decreased gradually to 80.2° in 10 min which ascribes to the lack of hydrophilic groups on the surface of CoNPA (Fig. 2a). After decorating an ultrathin TiO₂ layer that is rich in hydroxyl groups, the water contact angle of the resultant CoNPA@TiO₂ electrode had been largely reduced to 30.3° at the beginning of droplet contact with substrate, and further decreased to 22.1° after 10 min (Fig. 2b), indicating the high content of Ti-OH groups induced by ALD treatment to play a significant role in wettability improvement of CoNPA [60]. For CoNPA@Pt electrode that is only Pt nanoparticles anchored on CoNPA (Fig. 2c), the water contact angle also can be significantly reduced compared to that of CoNPA, but still much higher than that of CoNPA@TiO₂. In the case of CoNPA@TiO₂@Pt electrode, the water contact angle ranged from 30.8° to 23.7° (Fig. 2d), which was comparable with that of CoNPA@TiO₂ electrode. As a result, CoNPA@TiO₂@Pt electrode with such good wettability in cooperation with the potential HER contributions from well-dispersed Pt nanoparticles makes good HER activity be highly expected.

The composition and electronic structure of all CoNPA-based HER electrodes were further investigated by X-ray photoelectron spectroscopy (XPS) (Fig. 3). In comparison to CoNPA, the O 1s spectra (Fig. 3a) of both CoNPA@TiO₂ and CoNPA@TiO₂@Pt were deconvoluted into three peaks at $529.8, 531.6$, and 532.7 eV , respectively, which are corresponding to O^{2-} in TiO₂, hydroxyl group (OH^-), and adsorbed O on surface, respectively. In accordance with the result of the water contact angles evolution, the O 1s spectra reveal that hydroxyl groups are enriched on the surfaces of CoNPA@TiO₂ and CoNPA@TiO₂@Pt electrodes, thus endowing them with good wettability [44]. Whereas the CoNPA has only a broad tiny peak located in

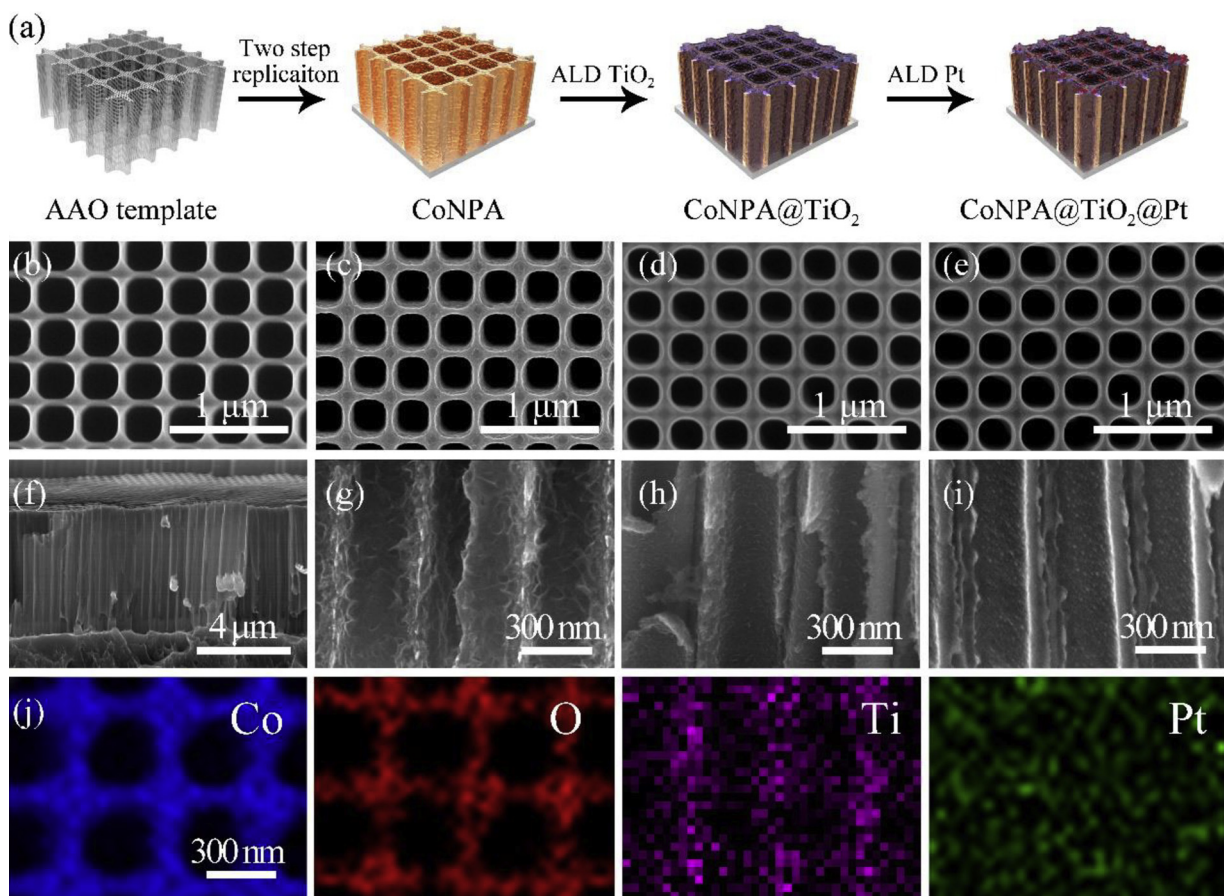


Fig. 1. (a) Schematic illustration of synthesis process for CoNPA@TiO₂@Pt HER electrode. Top-view SEM images of (b) initial AAO template, (c) CoNPA, (d) CoNPA@TiO₂, and (e) CoNPA@TiO₂@Pt. (f) Representative cross-sectional SEM view of CoNPA. The enlarged cross-sectional SEM images of (g) CoNPA, (h) CoNPA@TiO₂, and (i) CoNPA@TiO₂@Pt. (j) EDX elemental mapping of Co, O, Ti, and Pt of the as-prepared CoNPA@TiO₂@Pt electrode. The thickness of TiO₂ layer here is 3 nm.

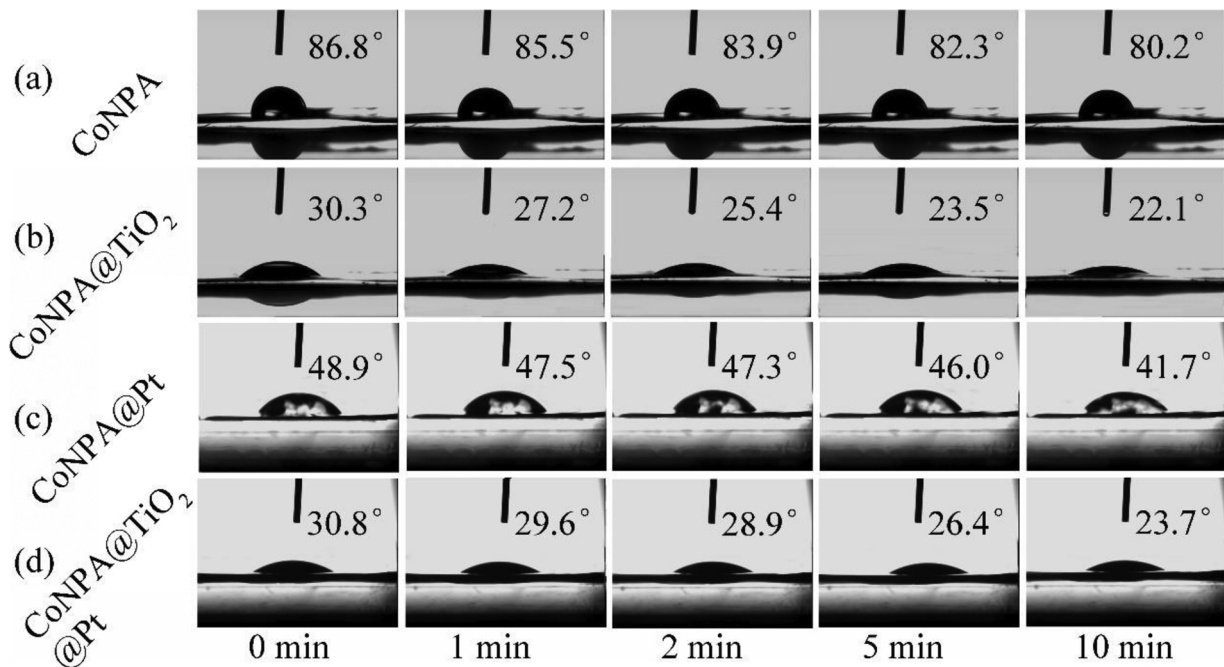


Fig. 2. Dynamic water contact measurement for (a) CoNPA, (b) CoNPA@TiO₂, (c) CoNPA@Pt, and (d) CoNPA@TiO₂@Pt from 0 to 10 min. The photograph at 0 min was taken immediately after resting the water droplet on the surface.

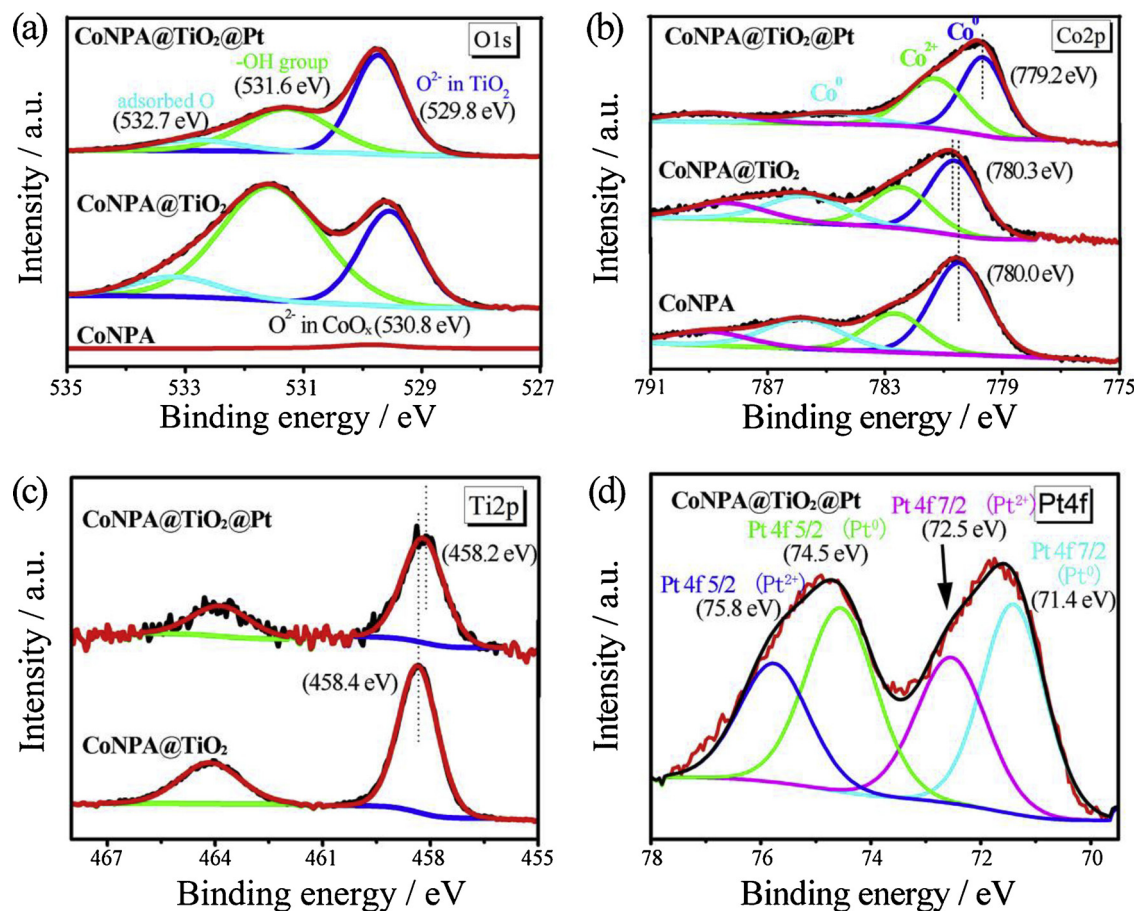


Fig. 3. XPS spectra of (a) O 1s, (b) Co 2p of CoNPA@TiO₂@Pt, CoNPA@TiO₂ and CoNPA. XPS spectra of (c) Ti 2p and (d) Pt 4f of CoNPA@TiO₂@Pt and CoNPA@TiO₂.

530.8 eV, which is attributed to the Co-O bond of CoO_x derived from the partial surface oxidation of CoNPA electrode. This also partially proves that the thin CoO_x layer alone is insufficient to increase the wettability of nanostructured electrode. It should be noted that the content of hydroxyl group may be consumed slightly during the deposition of Pt NPs. However, the resultant CoNPA@TiO₂@Pt electrode still possesses considerable hydroxyl groups and shows good hydrophilic characteristics. Thus the introduction of a thin layer of TiO₂ would be very necessary for the hydrophilic HER reaction to occur. As shown in Fig. 3b, the Co 2p peaks of CoNPA@TiO₂ slightly shift to a higher binding energy (780.3 eV) as compared with that of CoNPA (780.0 eV). On the contrary, the Co 2p peaks of CoNPA@TiO₂@Pt shift to a lower binding energy (779.2 eV) compared to that of CoNPA and CoNPA@TiO₂. Note that the obvious shifting of Co 2p peaks indicates that the ultrathin TiO₂ layer does not block the efficient charge transfer pathway from Co to Pt [61]. Thus, the unobstructed charge transport route would allow HER efficiently take place in Pt nanoparticles, benefiting to the improvement in the final HER efficiency with the HER contributions from both CoNPA and Pt nanoparticles. Moreover, the small shift of Ti 2p peak from 458.4 eV for CoNPA@TiO₂ to 458.2 eV for CoNPA@TiO₂@Pt (Fig. 3c) indicates TiO₂ to be negatively charged because of the strong electric interaction between Pt nanoparticles and TiO₂ layer [44]. The Pt 4f spectrum (Fig. 3d) shows doublets from the spin-orbit splitting of the 4f 7/2 and 4f 5/2 states, both of which can be deconvoluted into two peaks, revealing that the CoNPA@TiO₂@Pt catalysts consist of metallic Pt⁰ and Pt²⁺ [62]. It is worth mentioning that the existence of Pt²⁺ can be mainly ascribed to the very small size of Pt nanoparticles in an unsaturated coordination environment with a very high dispersion as well as low content, and further confirming the

strong interaction between the Pt nanoparticles and the CoNPA@TiO₂ support [63].

The HER activities of CoNPA@TiO₂@Pt electrode were studied in a standard three-electrode setup in an alkaline solution (1 M KOH). CoNPA, CoNPA@TiO₂, and CoNPA@Pt electrodes were also measured for comparison. Fig. 4a showed the LSV curves of all the four types of CoNPA-based HER electrodes. The onset potential defined as the potential reaching 1 mA cm⁻² for CoNPA@TiO₂@Pt electrode was 18 mV, which is much lower than that of CoNPA (106 mV), CoNPA@TiO₂ (28 mV), and CoNPA@Pt (22 mV), implying its outstanding HER activity. Also, CoNPA@TiO₂@Pt electrode displayed a relatively lower overpotential of 29 mV at the current density of 10 mA cm⁻², while that of Pt plate was 36 mV under the same conditions (Fig. S9). It suggests that the CoNPA@TiO₂@Pt electrode with ultralow Pt loading (54 μ g cm⁻² or 0.59 wt%) works better than that of thick Pt plate for catalytic reactions. The HER kinetics of all electrodes were evaluated by the corresponding Tafel plots within the overpotential range of 0–100 mV (Fig. 4b). Remarkably, the Tafel plots show that the dual-step surface engineering strategy efficiently decreased the Tafel slope of CoNPA@TiO₂@Pt electrode. The Tafel slope of 108 mV dec⁻¹ for CoNPA electrode indicates a typical Volmer–Heyrovsky route with the Volmer step as the rate-determining step. After modifying of thin layer of TiO₂/Pt NPs, the plot shows the slopes of 63 mV dec⁻¹, 58 mV dec⁻¹ and 42 mV dec⁻¹ for CoNPA@TiO₂, CoNPA@Pt and CoNPA@TiO₂@Pt electrodes, respectively. The low Tafel slopes of the CoNPA based electrodes suggest an effectively facilitated kinetics in the Volmer process. The smallest Tafel value of CoNPA@TiO₂@Pt electrode reveals that the HER activity on the CoNPA@TiO₂@Pt electrode follows a Volmer–Heyrovsky mechanism with the Heyrovsky (electrochemical

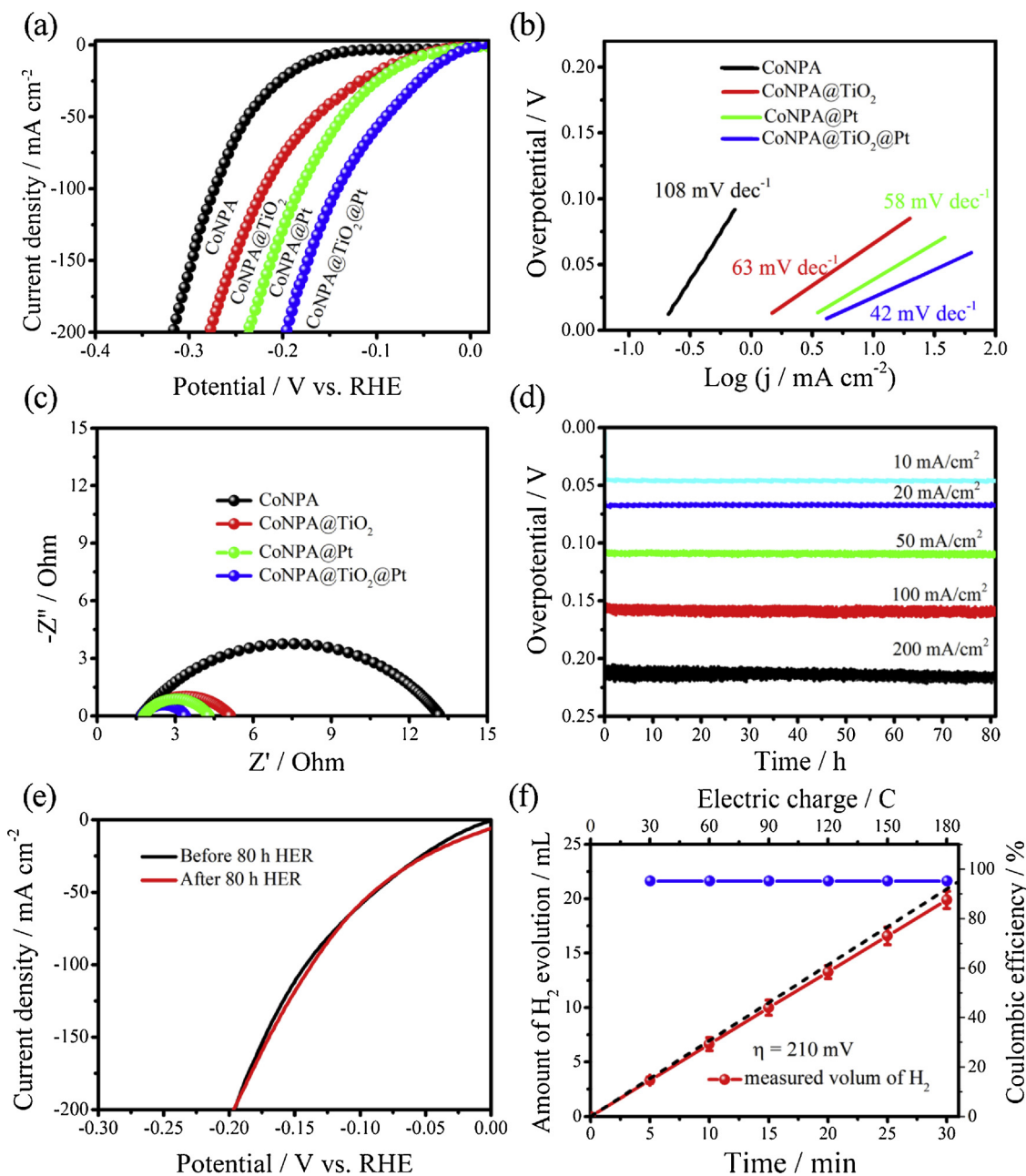


Fig. 4. Electrochemical performance. (a) Polarization curves, (b) Tafel plots, and (c) Nyquist plots of CoNPA, CoNPA@TiO₂, CoNPA@Pt, and CoNPA@TiO₂@Pt electrodes in 1 M KOH. (d) Chronoamperometric performance of CoNPA@TiO₂@Pt electrode operating at various current densities for 80 h. (e) Polarization curves of CoNPA@TiO₂@Pt electrode before and after 80 h HER. (f) The measured evolution H₂ versus reaction time and Coulomb by capturing evolved H₂ bubble in an inverted graduated cylinder from CoNPA@TiO₂@Pt electrode. The dotted line refers to the calculated theoretical value of H₂, and the blue line refers to the coulombic efficiency. The error bars arise from instrument uncertainty. (For interpretation of the references to colour in this figure legend, the reader is referred to the web version of this article.)

desorption) as the rate-determining step [64,65]. In comparison with the pristine CoNPA electrode, it could be concluded that the surface engineering steps could gradually change the rate-determining step of the HER approach, *i.e.*, shifting from Volmer gradually to Heyrovsky route. These results strongly reveal the synergistic contributions of ultrathin TiO₂ layer and well-dispersed Pt nanoparticles in promoting the HER activity. Moreover, the HER activity of CoNPA@TiO₂@Pt is also among the best one of recently developed HER electrodes as summarized in Table S2. Electrochemical impedance spectroscopy (EIS) measurements from 100 MHz to 0.01 Hz were performed to further evaluate the HER kinetics on different electrodes with applying an overpotential of 150 mV. As shown in the Nyquist plots (Fig. 4c), the charge transfer

resistance of CoNPA@TiO₂@Pt (1.7 Ω) is the lowest one among all CoNPA-based HER electrodes, while 13 Ω for CoNPA, 3.8 Ω for CoNPA@TiO₂, and 2.9 Ω for CoNPA@Pt. The smallest charge transfer resistance demonstrates the most effective charge transfer in CoNPA@TiO₂@Pt electrode, which results in faster electron transfer during HER process and thus leading to the best performance. Furthermore, the higher density of the active sites on CoNPA@TiO₂@Pt electrode, which was revealed by the larger electrochemically active surface area (ECSA) than that on other three electrodes through measuring the electrochemical double layer capacitance (Fig. S10), is believed to be responsible for the promising HER activity of CoNPA@TiO₂@Pt electrode. For instance, at an overpotential of 200 mV, the specific activity

(based on ECSA surface area, Table S1) for CoNPA@TiO₂@Pt electrode was found to be 0.88 mA cm⁻², outperforming other studied electrodes. These results suggest that the CoNPA@TiO₂@Pt electrode could serve as an efficient electrocatalyst to drive the hydrogen evolution reaction with high efficiency.

The electrochemical stability of the CoNPA@TiO₂@Pt electrode was firstly evaluated by multi-step chronoamperometric curves with overpotential increasing from 0 to 400 mV and an increment of 50 mV per hour (Fig. S11). The current remained stable over a wide potential range and rapid current response also indicates good mass transport and robustness of CoNPA@TiO₂@Pt electrode. The chronoamperometry characterizations for CoNPA@TiO₂@Pt electrode were further carried out at the current densities of 10, 20, 50, 100 and 200 mA cm⁻², respectively, for 80 h, and consequently the overpotentials almost remain quite stable at the various current densities as shown in Fig. 4d (e.g. the overpotential increase of only 4.1% at 200 mA cm⁻² for 80 h), further indicating long-term HER catalytic stability of CoNPA@TiO₂@Pt electrode. Moreover, negligible changes can be seen for CoNPA@TiO₂@Pt electrode from the polarization curves (Fig. 4e), the morphology (Fig. S12), as well as Co 2p and Pt 4f spectra (Fig. S13) before and after HER process of 80 h, again demonstrating the long-term stability of CoNPA@TiO₂@Pt electrode. Quantitative yield measurements were performed by capturing evolved large quantities of hydrogen bubble in an inverted graduated cylinder from CoNPA@TiO₂@Pt electrode (Fig. S14 and Movie S1). When 180 C of charge were passed through CoNPA@TiO₂@Pt electrode at overpotential of 210 mV for 30 min, the measured hydrogen yield was 19.9 ± 0.5 mL. The measured hydrogen yield is comparable to the theoretical H₂ yield (20.9 mL) based on the cathode (reduction) reaction: 2H₂O(l) + 2e⁻ → H₂(g) + 2OH⁻(aq). Therefore the quantitative Faradaic efficiency was ~95% (Fig. 4f).

The change of the surface hydrophilic nature of the electrocatalysts can efficiently facilitate HER by optimizing the free energy of hydrogen adsorption (ΔG_{H^*}). It is well known that the whole HER process in an alkaline medium consists of the three steps: (1) the initial electrocatalyst-water system, (2) intermediate electrocatalyst-H^{*} system, and (3) final electrocatalyst-H₂ system, of which the Gibbs free energy of catalyst-H^{*} (ΔG_{H^*}) reflects the moderate H chemisorption and releasing ability. Here density functional theory (DFT) calculations were applied to calculate the ΔG_{H^*} of CoNPA-based electrodes, which can give firm

theoretical proof and a direct explanation for the good HER performance. The ΔG_{H^*} calculation results based on the corresponding lattice models (Figs. S15–18) are shown in Fig. 5a. It was found that the ΔG_{H^*} of CoNPA@TiO₂@Pt is -0.04 eV, which is close to 0 eV compared with CoNPA@Pt (-0.38 eV), CoNPA@TiO₂ (-0.64 eV), and CoNPA (-0.99 eV) electrodes. It is worth mentioning that in the case of the large value of ΔG_{H^*} , it would be difficult to absorb H^{*} on the surface of electrocatalysts, on the contrary if the value is too small, the absorbed H^{*} would hardly desorb to evolve H₂, and tends to occupy the active sites and poison the HER process. Therefore, it is desirable to employ the value of $|\Delta G_{H^*}|$ to depict the HER activity of a series of electrocatalysts [3,66,67]. For instance, the value of $|\Delta G_{H^*}| \rightarrow 0$ for CoNPA@TiO₂@Pt defines the ease of a mediated adsorption-desorption behavior occurs on the surface of CoNPA@TiO₂@Pt electrode, which largely boost its electrocatalytic activities toward HER performance. The theoretical simulations are well in accordance with the experimental results, which CoNPA@TiO₂@Pt electrode has the best HER activity. Densities of state (DOS) were calculated to further pinpoint the origin of fast electron transfer of CoNPA@TiO₂@Pt. As shown in Fig. 5b, the band structure of total DOS survey are consecutive near the Fermi level, which demonstrates that CoNPA@TiO₂@Pt is intrinsically metallic. The DOS profile of Co illustrates that the d-orbitals of Co make a major contribution to the total DOS. However, TiO₂ barely contribute to DOS at Fermi level, which suggests more electron transport of Co than those of TiO₂ layer to the Pt nanoparticles, and it also suggests that the TiO₂ layer does not hinder the charge transportation which has been experimentally reflected by XPS results. The electron accumulation on Pt nanoparticles benefits to enhancing the kinetic process of electrochemical desorption process, since Heyrovsky reaction is the rate-controlling step, thus facilitating the overall HER kinetics.

On the basis of all results discussed above, a schematic illustration was proposed to illustrate the HER multi-step electrochemical process taking place on the surface of CoNPA@TiO₂@Pt electrode in an alkaline solution (Fig. 5c), including water adsorption, water activation, and electrochemical desorption of H₂. The first two steps belong to Volmer reaction, and the last process follows the rate-determining Heyrovsky reaction. Notably, these pathways depend largely on the inherent electronic and chemical properties of electrocatalyst surface. Compared with CoNPA pristine electrocatalyst, the dual-step surface engineering would be a desirable measure to improve the sluggish HER kinetics on

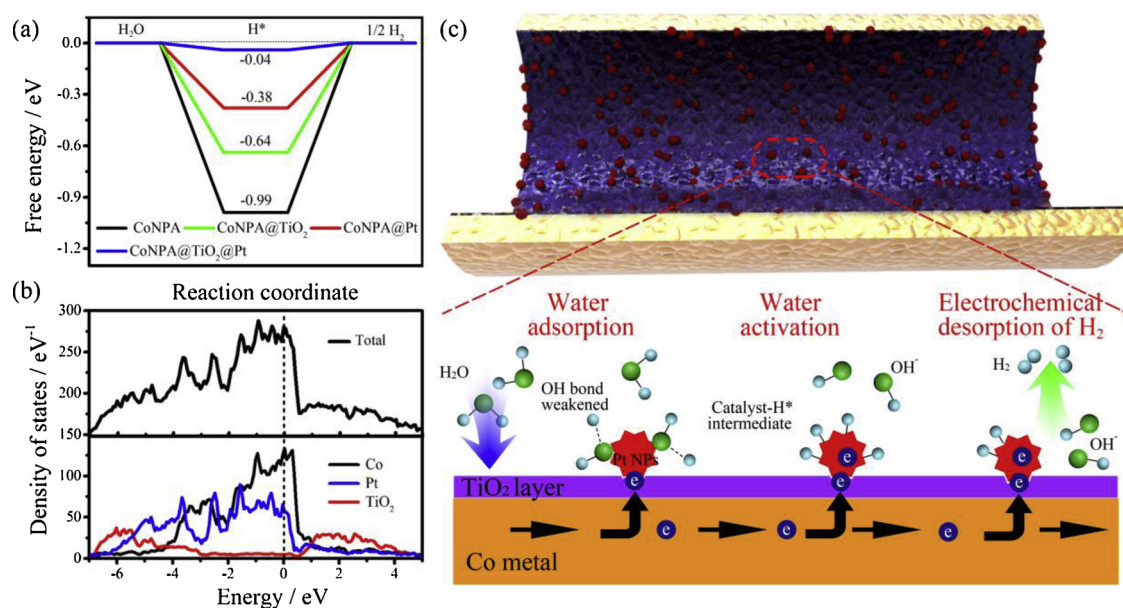


Fig. 5. Insight into the mechanism of HER process occurring on the surface of CoNPA@TiO₂@Pt electrodes. (a) Gibbs free energy diagram for CoNPA, CoNPA@TiO₂, CoNPA@Pt, and CoNPA@TiO₂@Pt. (b) Computed electronic density of states profile of CoNPA@TiO₂@Pt electrode. (c) Schematic illustration of water adsorption, water activation, and hydrogen generation process taking place inside the pore structure of CoNPA@TiO₂@Pt electrode.

CoNPA electrode, which can facilitate different parts of the overall multistep HER process by different components. For instance, the TiO_2 nanolayer and Pt NPs could effectively promote water adsorption and optimize the free energy of hydrogen adsorption and desorption, respectively. In comparison, the mechanisms of CoNPA and CoNPA-based electrodes, besides CoNPA@ TiO_2 @Pt, are illustrated in Fig. S19. They remained difficulties in improving the HER kinetics in alkaline electrolyte in terms of Volmer step, which contributing to the sluggish kinetics and inferior HER activity. The enhanced HER activity of CoNPA@ TiO_2 @Pt electrode can be attributed to the following reasons: (i) the conductive 3D network of CoNPA facilitates the charge transport throughout the entire nanoporous architecture to gain access to the internal reactive surface during the HER process (Fig. 5c) [68]; (ii) the conformal decoration of an ultrathin TiO_2 layer enriches the surface of CoNPA with hydroxyl groups, thus enables expose more water-accessible active centers to promote the Volmer step of HER, and meanwhile the ultrathin TiO_2 layer does not block the efficient charge transfer pathway from Co to Pt during the HER process; (iii) the well-dispersed Pt nanoparticles anchored on TiO_2 layer can supply more surface active sites without scarifying the improved wettability, and most importantly, they can activate the absorbed water molecules effectively to weaken $-\text{OH}$ bond for the generation of $\text{Pt}-\text{H}^*$ intermediates and then through electrochemical (Heyrovsky reaction) to evolve H_2 gas [4,12,36]; (iv) the open-channels of CoNPA allow the easy release of the evolved H_2 gas, and the robust structure of CoNPA endows CoNPA@ TiO_2 @Pt electrode with long-term performance and structure stability.

4. Conclusion

In summary, we demonstrated a dual-step surface engineering strategy toward improving the HER performance of nanoporous HER electrodes. With CoNPA as the representative nanoporous HER electrode, an ultrathin TiO_2 layer with an optimized thickness was conformally coated onto CoNPA to improve the wettability, and a well-dispersed Pt nanoparticles with an ultralow mass loading (*ca.* 54 $\mu\text{g cm}^{-2}$) was further anchored on TiO_2 layer to increase active sites and meanwhile to enhance the HER activity. The nanoporous electrode with open-channels structure of CoNPA not only supplied a large number of accessible active sites, but also effectively promoted the electron and mass transport as well as gas release. Together with the synergistic contributions from ultrathin TiO_2 layer and well-dispersed Pt nanoparticles, the present CoNPA@ TiO_2 @Pt electrode exhibited outstanding HER performance in alkaline conditions, in terms of the catalytic current density of 10 mA cm^{-2} at an ultralow overpotential of 29 mV, a long-term performance and structure stability. Noteworthy, this dual-step surface engineering strategy is not limited to the rational design and nanoengineering of HER electrodes, and similar strategy is also expected to be further applied to optimize nanoarchitected electrodes for other electrochemical energy conversion and storage devices.

Acknowledgements

L.L. and D.L. contributed equally to this work. The authors acknowledge funding from European Research Council (ThreeDsurface: 240144), European Research Council (HiNaPc: 737616), State of Thuringia and European Union (12021-715), BMBF (ZIK-3DNanoDevice: 03Z1MN11), German Research Foundation (DFG: LE 2249/4-1 and LE 2249/5-1), National Natural Science Foundation of China (21477050, 21522603, 21606111), and Natural Science Foundation of Jiangsu Province (BK20150482). Long Liu appreciates the China Scholarship Council (CSC) for providing a doctoral scholarship.

Appendix A. Supplementary data

Supplementary material related to this article can be found, in the online version, at doi:<https://doi.org/10.1016/j.apcatb.2018.11.036>.

References

- [1] J.A. Turner, *Science* 305 (2004) 972–974.
- [2] X. Zou, Y. Zhang, *Chem. Soc. Rev.* 44 (2015) 5148–5180.
- [3] J. Greeley, T.F. Jaramillo, J. Bonde, I. Chorkendorff, J.K. Nørskov, *Nat. Mater.* 5 (2006) 909.
- [4] J. Durst, A. Siebel, C. Simon, F. Hasche, J. Herranz, H. Gasteiger, *Energy Environ. Sci.* 7 (2014) 2255–2260.
- [5] J. Zhang, T. Wang, P. Liu, Z. Liao, S. Liu, X. Zhuang, M. Chen, E. Zschech, X. Feng, *Nat. Commun.* 8 (2017) 15437.
- [6] X.Y. Yu, Y. Feng, Y. Jeon, B. Guan, X.W.D. Lou, U. Paik, *Adv. Mater.* 28 (2016) 9006–9011.
- [7] S. Li, Y. Wang, S. Peng, L. Zhang, A.M. Al-Enizi, H. Zhang, X. Sun, G. Zheng, *Adv. Energy Mater.* 6 (2015) 1501661.
- [8] Y. Shen, Y. Zhou, D. Wang, X. Wu, J. Li, J. Xi, *Adv. Energy Mater.* 8 (2017) 1701759.
- [9] J.M. McEnaney, T.L. Soucy, J.M. Hodges, J.F. Callejas, J.S. Mondschein, R.E. Schaak, *J. Mater. Chem. A* 4 (2016) 3077–3081.
- [10] C. Yuan, H.B. Wu, Y. Xie, X.W.D. Lou, *Angew. Chem. Int. Ed.* 53 (2014) 1488–1504.
- [11] X. Yan, L. Tian, M. He, X. Chen, *Nano Lett.* 15 (2015) 6015–6021.
- [12] H. Jin, J. Wang, D. Su, Z. Wei, Z. Pang, Y. Wang, J. Am. Chem. Soc. 137 (2015) 2688–2694.
- [13] L. Yu, H. Zhou, J. Sun, F. Qin, F. Yu, J. Bao, Y. Yu, S. Chen, Z. Ren, *Energy Environ. Sci.* 10 (2017) 1820–1827.
- [14] U. Gupta, C. Rao, *Nano Energy* 41 (2017) 49–65.
- [15] C. Yang, M. Gao, Q. Zhang, J. Zeng, X. Li, A. Abbott, *Nano Energy* 36 (2017) 85–94.
- [16] M.S. Faber, R. Dziedzic, M.A. Lukowski, N.S. Kaiser, Q. Ding, S. Jin, *J. Am. Chem. Soc.* 136 (2014) 10053–10061.
- [17] Z. Wu, B. Fang, A. Bonakdarpour, A. Sun, D.P. Wilkinson, D. Wang, *Appl. Catal. B* 125 (2012) 59–66.
- [18] T.-W. Lin, C.-J. Liu, J.-Y. Lin, *Appl. Catal. B* 134 (2013) 75–82.
- [19] L. Wei, Y. Chen, Y. Lin, H. Wu, R. Yuan, Z. Li, *Appl. Catal. B* 144 (2014) 521–527.
- [20] C. Liu, L. Wang, Y. Tang, S. Luo, Y. Liu, S. Zhang, Y. Zeng, Y. Xu, *Appl. Catal. B* 164 (2015) 1–9.
- [21] Y. Shi, B. Zhang, *Chem. Soc. Rev.* 45 (2016) 1529–1541.
- [22] Y. Pei, Y. Yang, F. Zhang, P. Dong, R. Baines, Y. Ge, H. Chu, P.M. Ajayan, J. Shen, M. Ye, *ACS Appl. Mater. Interfaces* 9 (2017) 31887–31896.
- [23] Q. Liu, J. Tian, W. Cui, P. Jiang, N. Cheng, A.M. Asiri, X. Sun, *Angew. Chem. Int. Ed.* 126 (2014) 6828–6832.
- [24] K. Xu, H. Cheng, H. Lv, J. Wang, L. Liu, S. Liu, X. Wu, W. Chu, C. Wu, Y. Xie, *Adv. Mater.* 30 (2017) 1703322.
- [25] W. Cui, Q. Liu, Z. Xing, A.M. Asiri, K.A. Alamry, X. Sun, *Appl. Catal. B* 164 (2015) 144–150.
- [26] Y. Zhong, X. Xia, F. Shi, J. Zhan, J. Tu, H.J. Fan, *Adv. Sci.* 3 (2016) 1500286.
- [27] W.-F. Chen, J.T. Muckerman, E. Fujita, *Chem. Commun.* 49 (2013) 8896–8909.
- [28] Y.N. Regmi, G.R. Waetzig, K.D. Duffee, S.M. Schmoecker, J.M. Thode, B.M. Leonard, *J. Mater. Chem. A* 3 (2015) 10085–10091.
- [29] F. Harnisch, G. Sievers, U. Schröder, *Appl. Catal. B* 89 (2009) 455–458.
- [30] S. Carenco, D. Portehault, C. Boissiere, N. Mezailles, C. Sanchez, *Chem. Rev.* 113 (2013) 7981–8065.
- [31] C.G. Morales-Guio, L.-A. Stern, X. Hu, *Chem. Soc. Rev.* 43 (2014) 6555–6569.
- [32] L. Liu, X. Yang, N. Ma, H. Liu, Y. Xia, C. Chen, D. Yang, X. Yao, *Small* 12 (2015) 1295–1301.
- [33] M.S. Faber, S. Jin, *Energy Environ. Sci.* 7 (2014) 3519–3542.
- [34] P. Chen, K. Xu, S. Tao, T. Zhou, Y. Tong, H. Ding, L. Zhang, W. Chu, C. Wu, Y. Xie, *Adv. Mater.* 28 (2016) 7527–7532.
- [35] R. Subbaraman, D. Tripkovic, D. Stremmek, K.-C. Chang, M. Uchimura, A.P. Paulikas, V. Stamenkovic, N.M. Markovic, *Science* 334 (2011) 1256–1260.
- [36] Y. Zheng, Y. Jiao, M. Jaroniec, S.Z. Qiao, *Angew. Chem. Int. Ed.* 54 (2015) 52–65.
- [37] J. Kibsgaard, Z. Chen, B.N. Reinecke, T.F. Jaramillo, *Nat. Mater.* 11 (2012) 963.
- [38] H. Zhao, L. Liu, R. Vellacheri, Y. Lei, *Adv. Sci.* 4 (2017) 1700188.
- [39] Y. Mi, L. Wen, Z. Wang, D. Cao, Y. Fang, Y. Lei, *Appl. Catal. B* 176 (2015) 331–337.
- [40] D.R. Rolison, J.W. Long, J.C. Lytle, A.E. Fischer, C.P. Rhodes, T.M. McEvoy, M.E. Bourg, A.M. Lubers, *Chem. Soc. Rev.* 38 (2009) 226–252.
- [41] Z. Gao, Y. Qin, *Acc. Chem. Res.* 50 (2017) 2309–2316.
- [42] L. Mi, J. Yu, F. He, L. Jiang, Y. Wu, L. Yang, X. Han, Y. Li, A. Liu, W. Wei, *J. Am. Chem. Soc.* 139 (2017) 10441–10446.
- [43] C. Meng, B. Wang, Z. Gao, Z. Liu, Q. Zhang, J. Zhai, *Sci. Rep.* 7 (2017) 41825.
- [44] J.X. Feng, H. Xu, Y.T. Dong, X.F. Lu, Y.X. Tong, G.R. Li, *Angew. Chem. Int. Ed.* 129 (2017) 3006–3010.
- [45] E.S. Andreiadis, P.-A. Jacques, P.D. Tran, A. Leyris, M. Chavarot-Kerlidou, B. Jousselle, M. Matheron, J. Pécaut, S. Palacin, M. Fontecave, *Nat. Chem.* 5 (2013) 48–53.
- [46] H. Zhao, C. Wang, R. Vellacheri, M. Zhou, Y. Xu, Q. Fu, M. Wu, F. Grote, Y. Lei, *Adv. Mater.* 26 (2014) 7654–7659.
- [47] Z. Zhan, Y. Lei, *ACS Nano* 8 (2014) 3862–3868.
- [48] M. Wu, L. Wen, Y. Lei, S. Ostendorp, K. Chen, G. Wilde, *Small* 6 (2010) 695–699.
- [49] L. Wen, Y. Mi, C. Wang, Y. Fang, F. Grote, H. Zhao, M. Zhou, Y. Lei, *Small* 10 (2014) 3162–3168.

[50] S. Gao, Y. Lin, X. Jiao, Y. Sun, Q. Luo, W. Zhang, D. Li, J. Yang, Y. Xie, *Nature* 529 (2016) 68–71.

[51] G. Kresse, J. Furthmüller, *Phys. Rev. B* 54 (1996) 11169.

[52] P.E. Blöchl, *Phys. Rev. B* 50 (1994) 17953.

[53] G. Kresse, D. Joubert, *Phys. Rev. B* 59 (1999) 1758.

[54] Z. Wang, D. Cao, L. Wen, R. Xu, M. Obergfell, Y. Mi, Z. Zhan, N. Nasori, J. Demsar, Y. Lei, *Nat. Commun.* 7 (2016) 10348.

[55] L. Wen, Z. Wang, Y. Mi, R. Xu, S.H. Yu, Y. Lei, *Small* 11 (2015) 3408–3428.

[56] Y. Mi, L. Wen, Z. Wang, D. Cao, H. Zhao, Y. Zhou, F. Grote, Y. Lei, *Catal. Today* 262 (2016) 141–145.

[57] M. Li, Q. Ma, W. Zi, X. Liu, X. Zhu, S.F. Liu, *Sci. Adv.* 1 (2015) e1400268.

[58] L. Liu, H. Hou, L. Wang, R. Xu, Y. Lei, S. Shen, D. Yang, W. Yang, *Nanoscale* 9 (2017) 15650–15657.

[59] Y.W. Chen, J.D. Prange, S. Dühnen, Y. Park, M. Gunji, C.E. Chidsey, P.C. McIntyre, *Nat. Mater.* 10 (2011) 539–544.

[60] K. Liu, M. Cao, A. Fujishima, L. Jiang, *Chem. Rev.* 114 (2014) 10044–10094.

[61] B.Y. Xia, H.B. Wu, N. Li, Y. Yan, X.W.D. Lou, X. Wang, *Angew. Chem. Int. Ed.* 127 (2015) 3868–3872.

[62] J. Zhang, C. Chen, S. Chen, Q. Hu, Z. Gao, Y. Li, Y. Qin, *Catal. Sci. Technol.* 7 (2017) 322–329.

[63] J. Luo, H. Tang, X. Tian, S. Hou, X. Li, L. Du, S. Liao, *ACS Appl. Mater. Interfaces* 10 (2018) 3530–3537.

[64] X. Gao, H. Zhang, Q. Li, X. Yu, Z. Hong, X. Zhang, C. Liang, Z. Lin, *Angew. Chem. Int. Ed.* 55 (2016) 6290–6294.

[65] B. Conway, B. Tilak, *Electrochim. Acta* 47 (2002) 3571–3594.

[66] R. Wu, J. Zhang, Y. Shi, D. Liu, B. Zhang, *J. Am. Chem. Soc.* 137 (2015) 6983–6986.

[67] J.K. Nørskov, T. Bligaard, J. Rossmeisl, C.H. Christensen, *Nat. Chem.* 1 (2009) 37.

[68] L. Liu, H. Zhao, Y. Wang, Y. Fang, J. Xie, Y. Lei, *Adv. Funct. Mater.* 28 (2018) 1705107.